RESEARCH PAPER

Keyhole TIG welding of newly developed nickel-based superalloy VDM Alloy 780

Achmad Ariaseta[1,2] · Nima Sadeghinia[1] · Joel Andersson[1] · Olanrewaju Ojo[3]

Abstract

The influence of keyhole TIG (K-TIG) welding parameters on the weld geometry and defects of a new nickel-based superalloy VDM Alloy 780 alloy were investigated using a statistical design of experiment, and the microstructures of the heat-affected zone (HAZ) and fusion zone (FZ) of the K-TIG-welded VDM Alloy 780 were characterized. No cracks are found in the FZ and HAZ. Travel speed significantly influences the minimum weld width (Wm), face and root excess weld metal, face underfill, and average pore diameter. Welding current and the interaction current*travel speed significantly influence the face and root excess weld metals, respectively. Interdendritic microconstituents in the FZ are identified as (Nb,Ti)C particles and γ/Laves eutectic constituents based on SEM–EDS analysis. In addition, plate-like precipitates likely to be δ/η phase are observed surrounding the interdendritic Laves eutectics, and γ′ precipitates are found to be inhomogeneously precipitated in the FZ. In the partially melted zone (PMZ), (Nb,Ti)C, Laves phase, and plate-like particles are found in the liquated and resolidified regions. Constitutional liquation of (Nb,Ti)C in HAZ is observed where the liquated (Nb,Ti)C appears to be associated with the γ/Laves eutectic as a resolidified product.

Keywords K-TIG welding · Weld geometry · Weld defects · Microstructure · VDM Alloy 780 superalloy

1 Introduction

VDM Alloy 780 is a newly patented wrought -strengthened Ni-based superalloy that VDM Metals have recently developed to improve the maximum service temperature while maintaining the excellent processability of Alloy 718 [1–3]. This new alloy is intended for high-temperature applications such as gas turbine components in aircraft engines with service temperature requirements of up to about 750 °C. The development of VDM Alloy 780 is accomplished by

Recommended for publication by Commission IX—Behaviour of Metals Subjected to Welding

✉ Achmad Ariaseta
   achmad.ariaseta@hv.se

1 Department of Engineering Science, University West, 46186 Trollhätan, Sweden

2 Department of Metallurgical Engineering, Faculty of Mining and Petroleum Engineering, Institut Teknologi Bandung, Jl. Ganesha 10, Bandung 40132, Indonesia

3 Department of Mechanical Engineering, University of Manitoba, Winnipeg, MB R3T 5V6, Canada

having substantial distinctions to Alloy 718 in the alloy chemical composition, which are the addition of 25% Co substituting Fe and, to some extent, Ni, improved amount of Al (2% instead of ~0.6%), decreased amount of Ti (0.2% instead ~0.94%) [4, 5]. The amounts of Nb, Cr, and Mo are similar to Alloy 718. The alloy design strategy yields in the γ′ phase being the main hardening phase, which improves its thermal stability compared to Alloy 718, which is hardened by γ″.

The new alloy VDM Alloy 780 is a promising material candidate to be utilized in the hot sections of aero engines, which have been preferably fabricated by joining small pieces of superalloys by welding process instead of casting single large parts. This type of fabrication strategy has several benefits, such as increasing the design flexibilities, e.g., it becomes possible to join cast (complex geometry) alloys with wrought (high strength) alloys and join different superalloys [6]. Another advantage is reducing the component's total weight, enhancing the engine's fuel efficiency, and eventually less CO_2 emission to the environment.

In the fabrication of structural components of the jet engine in the aerospace industry, one of the most standard techniques employed in the fabrication is still gas tungsten

arc welding (GTAW) or tungsten inert gas (TIG) welding [7]. However, TIG welding processes have undergone notable improvements that paved the way for the fabrication of structural components of the jet engine, and now possible to use lower heat input. One of the most recent TIG welding processes, so-called keyhole TIG (K-TIG) welding, allows one to weld with lower heat input and faster travel speed to produce full penetration in a single-pass compared to the traditional TIG. The main difference between K-TIG and TIG welding is that K-TIG produces a more highly concentrated arc with higher energy density and arc pressure than the traditional TIG, which is the primary reason why K-TIG welding can achieve keyhole or full penetration in a single pass with a much faster travel speed [8–10].

The fundamental principle of the K-TIG welding process is explained as follows [9]. A cooling shoulder is attached to the standard tungsten electrode or TIG torch in K-TIG welding to substantially cool down the tungsten rod. The cathode area, i.e., the high-temperature region in the tungsten tip, is confined to a highly narrow region. The current density in the cathode region is thus enhanced, and the electromagnetic effect further increases arc compression. The entire arc jet diameter is restricted; hence, the arc pressure and energy density of the arc are enhanced. When the welding current is sufficiently high (above 300 A), the arc pressure is adequately strong to overcome the surface tension of the molten pool; the melted metal is expelled away, and then the formation of a keyhole occurs inside the weld pool. If the ability to penetrate by the arc is powerful enough, a full penetration by the keyhole in the workpiece will be achieved. This process superiority is essential when welding advanced materials such as superalloys in the jet engine. Moreover, K-TIG welding is much easier to operate and more cost-effective than other high-energy density welding processes, e.g., laser and electron beam welding [11], making it superbly suitable for on-site fabrication [12].

In welding superalloys, it is of paramount importance to produce a sound weld that meets the tight weld quality requirement in the aerospace industry in terms of weld geometry and weld defects. Moreover, understanding the microstructures in the HAZ and FZ is essential since they influence the properties and integrity of the weldment and

can become the foundation for developing a suitable post-weld heat treatment (PWHT) of the alloy. Since VDM Alloy 780 is a new alloy, no reports from the literature regarding the influence of K-TIG welding parameters on the weld geometry and defects and no knowledge available with regard to the resulting microstructures in HAZ and FZ of the welded alloy. Therefore, the aim in this article is to study the influence of K-TIG welding parameters on the weld geometry and defects when welding newly developed VDM Alloy 780 and to characterize the microstructures of welded alloy in the HAZ and FZ.

2 Experimental procedure

2.1 Material and welding

As-received VDM Alloy 780 plates in solution-annealed condition with the chemical composition (in wt%) shown in Table 1 and thickness of 5.7 mm were used for the bead-on-plate weld runs using the automatic K-TIG welding process. The chemical compositions were measured by optical emission analysis (Mg, P, and B), graphite furnace AAS (Sn, As, Pb, Se, Bi, Ag, and Te), X-ray fluorescence spectroscopy (Mo, Cr, Mn, Nb, Si, Ti, Fe, Al, Cu, W, V, Zr, and Co), inductive coupled plasma (Ta), flame AAS (Ca), and combustion analysis (N, S, O, and C). High-purity argon gas, 99.99%, was used as the shielding gas, with a 10 l/min flow rate. The schematic of the bead-on-plate weld run on the VDM Alloy 780 plates is shown in Fig. 1.

2.2 Statistical design of experiment

The design of experiment (DOE) used in this study to investigate the effect of K-TIG welding process parameters on weld geometry and defects is based on a two-level full factorial design with the two factors, i.e., welding current and travel speed. The levels defined for process parameters with their notations, units, and levels for the K-TIG welding process are given in Table 2. The detail of sample numbers with the corresponding factors or welding parameters in the full factorial DOE runs is shown in Table 3. Here, Samples 5,

Table 1 Chemical compositions of alloy VDM Alloy 780 in wt% used in the present study

Element	Ni	Al	Ti	Nb	S	Cr	Sn	V	Zr	Mo	Co	Cu
wt%	Bal	2.19	0.30	5.39	0.0005	17.95	< 0.001	0.01	< 0.01	2.91	25.08	0.01
Element (cont.)	Si	Mn	C	P	Ta	Se	Mg	B	N	O	Fe	
wt% (cont.)	0.03	0.01	0.021	0.01	0.01	< 0.0003	0.0006	0.003	0.008	0.001	0.47	
Element (cont.)	W	Ca	Se	As	Sb	Ag	Te	Bi				
wt% (cont.)	0.02	0.002	< 0.0003	< 0.001	< 0.0005	< 0.0001	< 0.00005	< 0.00003				

Fig. 1 The schematic of bead-on-plate weld run on the VDM Alloy 780 plates and the corresponding location where the cross-sections were cut out
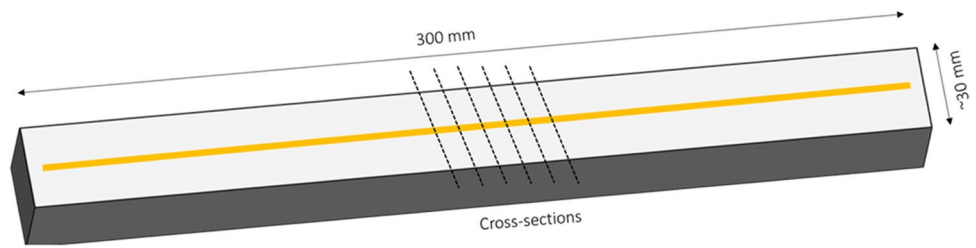

Table 2 K-TIG welding process parameters and their level used in this study

No	K-TIG welding parameters	Units	Process parameter levels		
			−1	0	1
1	Welding current	A	480	485	490
2	Travel speed	mm/s	8	8.5	9

Table 3 Full factorial DOE runs of K-TIG welding

Sample no	Current (A)	Travel speed (mm/s)
1	480	9
2	490	8
3	480	8
4	490	9
5	485	8.5
6	485	8.5
7	485	8.5

6, and 7 are the center points of the DOE runs. The welding current and travel speed ranges were chosen to achieve full penetration without burning through the plate. The distance between the electrode tip and the workpiece was kept at 1.5 mm throughout the DOE runs. After welding the samples, the typical features of weld geometry and defects stipulated in AWS D17.1 M:2010 [13] as the responses were measured in the as-welded alloy, i.e., underfill, excess weld metal on the face and root, and average pore diameter. In addition, measurements on minimum weld width (Wm) and cracks were also performed. However, no cracks are found in the HAZ and FZ of any sample. Then, the results were inputted into Modde software (MODDE 12, Umetrics, Umeå, Sweden). Linear regression is used to model each response according to Eq. (1) below.

$$y = \alpha_0 + \alpha_1 \text{current} + \alpha_2 \text{speed} + \alpha_{12}(\text{current})(\text{speed}) + \varepsilon \tag{1}$$

where y is the response and dependent variable; the α terms are constants, of which all except α_0 are called regression coefficients; ε is the error or modeling residual. The factor levels are represented on a coded scale. The welding current levels of 480, 485, and 490 A are coded − 1, 0,

and 1, respectively. The travel speed levels of 8, 8.5, and 9 mm/s are coded − 1, 0, and 1, respectively. The calculation of regression coefficients was performed in Modde using the multiple linear regression method, and a 95% confidence interval of these coefficients was also calculated. In addition, a square test was automatically performed in Modde to detect possible square terms or non-linearity in the regression models. The reproducibility test is also carried out in Modde by comparing the variation of replicates to the overall variability and assigned a value of 0–1 in Modde, wherein a value higher than 0.5 suggests good reproducibility [14]. Other diagnostic parameters, R^2 and p-value, are also calculated by the Modde.

2.3 Weld geometry and weld defects quantification

Five cross-sections transverse to the welding direction were cut out from all the bead-on-plate weld runs at the center of the plates (cf. Figure 1). The mounted cross-sections were prepared by multistep grinding with the grit sizes down to 52 μm, followed by three polishing steps with 9 μm and 3 μm diamond suspensions and 0.02 μm colloidal SiO_2. Electrolytic etching using 10% oxalic acid at 2.5 V was carried out to reveal the bead geometry. Macrographs of the sections were then taken on etched samples using a light optical microscope (LOM) to obtain precise measurements of Wm, underfill, and excess weld metal. The average values were obtained from five cross-sections. An example of a LOM image of weld bead geometry and the corresponding measurements is shown in Fig. 2. The average pore diameter was quantitatively measured using LOM on an as-polished surface in the whole FZ area of five cross-sections using ImageJ software.

The measured face underfill, face and root excess weld metal, and average pore diameter in the DOE runs were compared with the maximum acceptable limit stipulated in AWS D17.1 M:2010 [13]. Note that Wm is not specified in
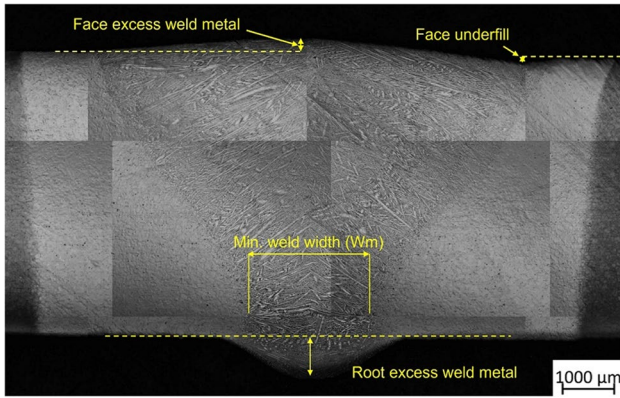
Fig. 2 OM image showing the example of weld bead geometry and the measurements

the AWS D17.1 M:2010. Therefore, 1.5 mm was used as the minimum acceptable value for Wm in aerospace applications as the reference [15].

2.4 Scanning electron microscopy (SEM) characterization

Microstructural characterization was performed on as-polished and electrolytically etched samples using a field

emission gun scanning electron microscope (FEG-SEM) operated in the in-lens and backscatter electron (BSE) modes at an accelerating voltage of 10–20 kV. The FEG-SEM was also equipped with Oxford energy-dispersive X-ray spectroscopy (EDS). The SEM characterization was performed on samples welded using the lowest (lowest current and fastest travel speed) and highest (highest current and lowest travel speed) heat inputs covered in the DOE. It is found that there are no notable microstructural differences in both of these welded samples; thereby, the welded samples produced in all DOE runs are assumed to exhibit a similar microstructure. Thus, the sample welded using the lowest heat input is presented in this article.

3 Results and discussion

3.1 Influence of K-TIG welding process parameters on weld geometry and weld defects

All measured responses of Samples 1–7 are depicted in Fig. 3. These data are taken directly from Table 4. The center points in all responses, i.e., Sample 5–7, show reasonably similar values. This is reflected in the calculated reproducibility value of 0.940, 0.856, 0.732, 0.938, and 0.984 for Wm, face and root excess weld metal, face underfill, and
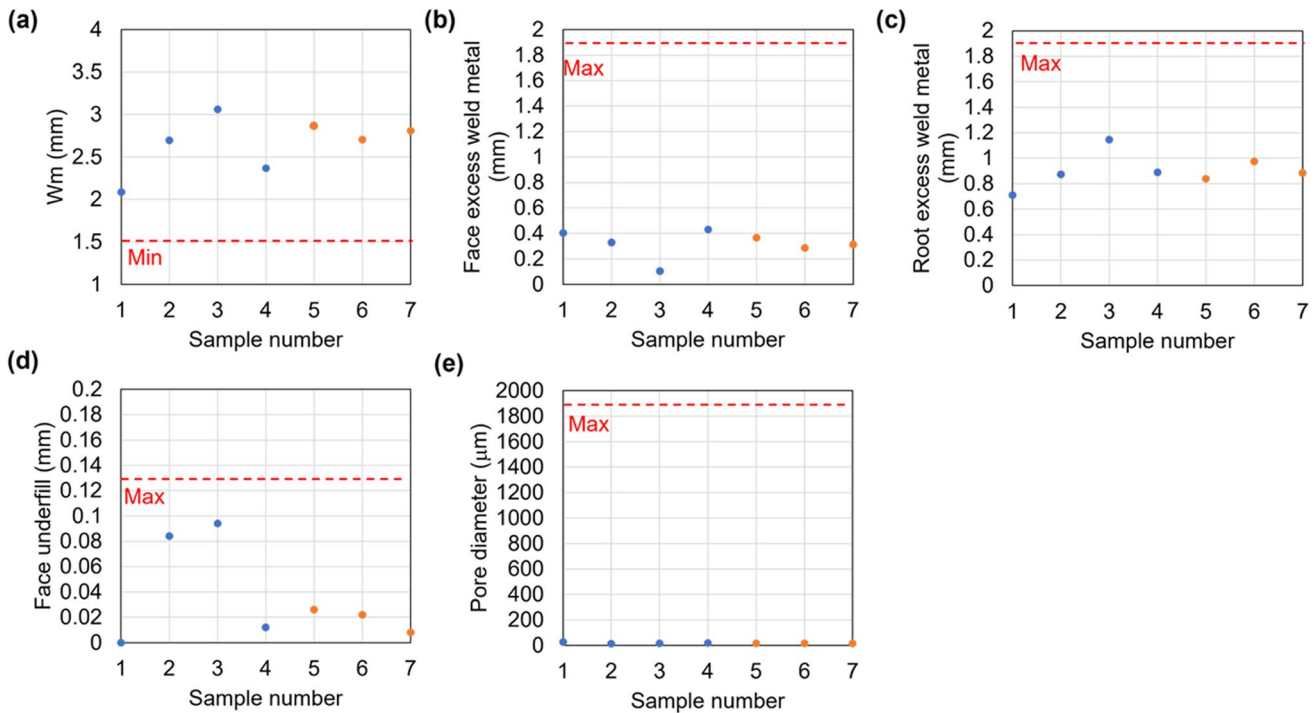

Fig. 3 Measured responses of K-TIG welded samples (samples with varied parameters are in blue, while replicates are in orange); measured face and root excess weld metal, face underfill, and average pore diameter are compared with the maximum acceptable limit specified in AWS D17.1 M:2010, while 1.5 mm is used as the minimum acceptable limit for Wm as a reference, shown in red dotted lines [15]

Table 4 The measured responses in all DOE runs of K-TIG welding

Sample no	Current (A)	Travel speed (mm/s)	Wm (mm)	Face underfill (mm)	Face excess weld metal (mm)	Root excess weld metal (mm)	Ave. pore diameter (μm)
1	480	9	2.09	0	0.40	0.71	27
2	490	8	2.64	0.08	0.33	0.87	13
3	480	8	3.18	0.09	0.10	1.15	16
4	490	9	2.37	0.01	0.43	0.89	18
5	485	8.5	2.86	0.02	0.37	0.84	16
6	485	8.5	2.75	0.03	0.29	0.97	16
7	485	8.5	2.81	0.01	0.31	0.88	15

average pore diameter, respectively. Moreover, all the DOE runs produced welds with Wm larger than 1.5 mm and excess weld metals, face underfill, and average pore diameter lower than the maximum allowable limit stipulated in AWS D17.1 M:2010 [13] for aerospace applications.

The analysis performed in Modde modeled the responses of the Wm, face and root excess weld metal, face underfill, and average pore diameter of the seven samples to know which parameters had the strongest influence on the responses and whether there are any substantial interactions among these parameters. Thus, regression coefficients and their 95% confidence interval are plotted in Fig. 4. The statistically significant parameters (p-value < 0.05) are marked in green, while those that are not statistically significant (p-value ≥ 0.05) that had zero included in their confidence intervals are marked in red. All the calculated p-values are shown in Table 5, where values lower than 0.05 are marked in bold. It is shown that travel speed significantly influences the Wm, face and root excess weld metal, face underfill, and average pore diameter. The current and interaction current*travel speed significantly influence the face and root excess weld metal, respectively.

The next step is to know the comparison between all the experimentally measured weld geometry and defects and the calculated results of the regression model. The regression models of Wm, face excess weld metal, root excess weld metal, face underfill, and average pore diameter are shown in Eqs. (2)–(6), respectively. No square terms or non-linearity is detected in all the response regression models based on the square test automatically carried out in Modde. Plots comparing the measured and calculated weld geometry and weld defects are presented in Fig. 5. The line crosses the points where the calculated values are equal to the measured values. The R^2 values of all measured responses are displayed in Table 5.

From Table 5, face and root excess weld metals exhibit high R^2 values of 0.91 and 0.95, respectively, indicating that the calculated results were close to the experimental results. It is seen that for face and root excess weld metal presented

in Fig. 5 that the points are crossed by the 1:1 line, indicating a good fit. The p-values of the face and root excess weld metals' regression models generated in the ANOVA table are 0.018 and 0.045, respectively (Table 5). This suggests that the regression models of face and root excess weld metal, as displayed in Eqs. (4) and (5), are statistically good or significant.

$$\text{Wm (mm)} = 2.847 - 0.021\text{current} - 0.327\text{speed} + 0.161(\text{current})(\text{speed}) \tag{2}$$

$$\text{Face excess weld (mm)} = 0.352 + 0.062\text{current} + 0.101\text{speed} - 0.050(\text{current})(\text{speed}) \tag{3}$$

$$\text{Root excess weld (mm)} = 0.959 - 0.024\text{current} - 0.106\text{speed} + 0.113(\text{current})(\text{speed}) \tag{4}$$

$$\text{Face underfill (mm)} = 0.035 + 0.001\text{current} - 0.042\text{speed} + 0.006(\text{current})(\text{speed}) \tag{5}$$

$$Ave.porediameter(\mu m) = 17.286 - 3.000current + 4.000speed - (current)(speed) \tag{6}$$

The R^2 values of Wm, face underfill, and average pore diameter, as displayed in Table 6, are 0.83, 0.81, and 0.88, respectively. Even though the R^2 values of the regression models are reasonably high in the range of 0.81–0.88, it can be seen from Fig. 5 that the calculated Wm, face underfill, and average pore diameter values did not accurately match the experimental results. The p-values of regression models of Wm, face underfill, and average pore diameter, as shown in Table 6, are 0.114, 0.332, and 0.065 indicating that the regression models displayed in Eqs. (2), (5, and (6) are statistically poor or not significant. The statistically poor models may explain the discrepancy between calculated and experimental values for Wm, face underfill, and average pore diameter, as shown in Fig. 5.
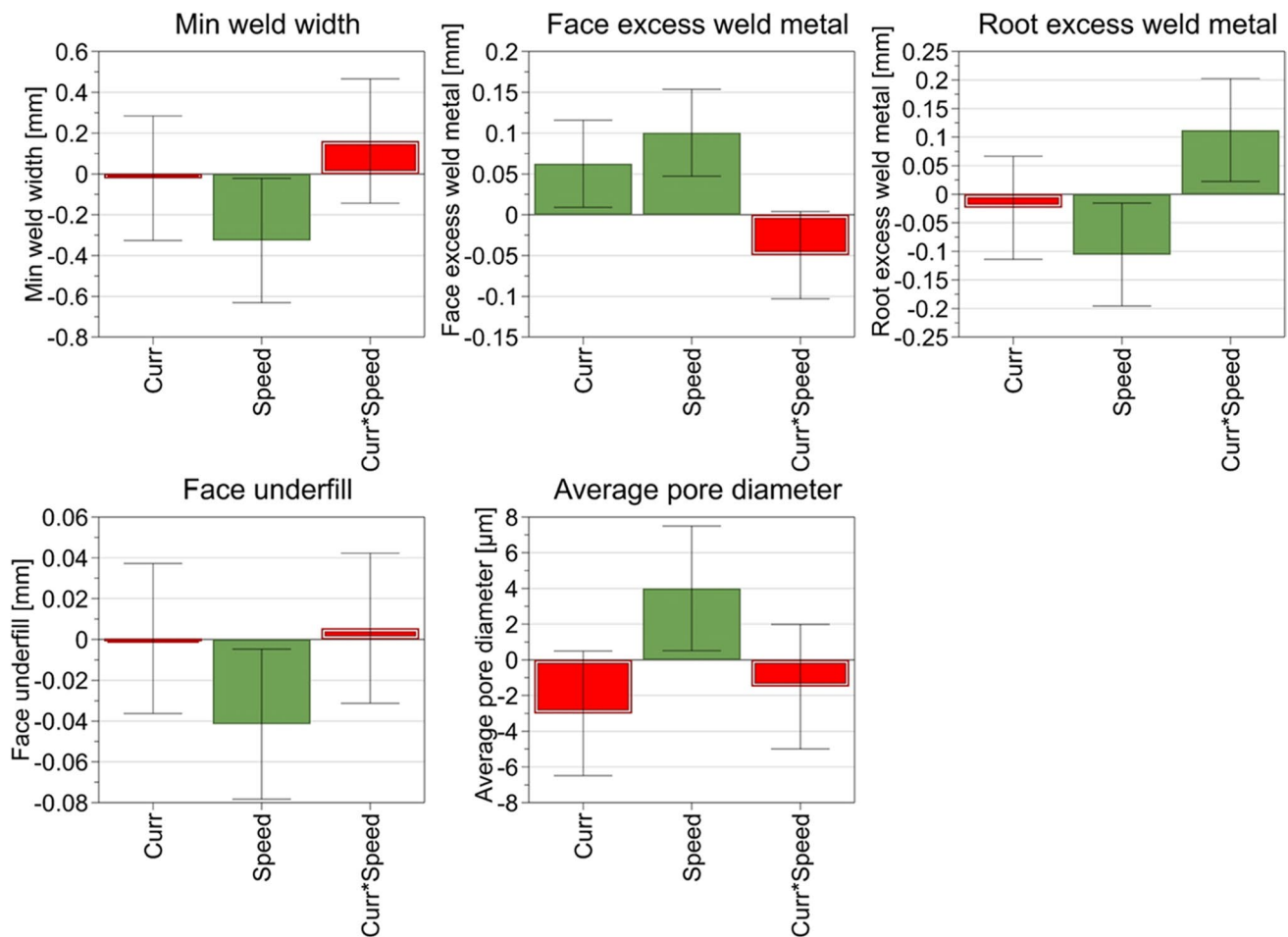
Fig. 4 Regression coefficients for different factors and interaction of factors affecting weld geometry and weld defects (green bars show significant factors, while red bars show non-significant factors)

Table 5 *p*-values calculated using Modde software for the regression constants that had significant (significant values are marked in bold) and non-significant influence on the responses (Wm, face and root excess weld metal, face underfill, and average pore diameter).

Factor	*p*-value of Wm	*p*-value of face excess weld metal	*p*-value of root excess weld metal	*p*-value of face underfill	*p*-value of ave. pore diameter
Current	0.839	**0.033**	0.468	0.969	0.072
Travel speed	**0.042**	**0.009**	**0.034**	**0.038**	**0.036**
Current*travel speed	0.191	0.060	**0.029**	0.667	0.265

Moreover, it is apparent in Fig. 5 for face underfill that negative values are predicted. This does not, however, mean that negative face underfill exists. In reality, the measured values are near zero, which along with a lack of fit, make it numerically possible to predict negative values. From the constructed ANOVA table, it is seen that the regression model of face underfill has a significant lack of fit.

3.2 SEM microstructural characterization

3.2.1 Base material microstructure

The primary microstructural features of the VDM Alloy 780 base materials are depicted in the low magnification backscatter electron (BSE) image in Fig. 6a. The average grain
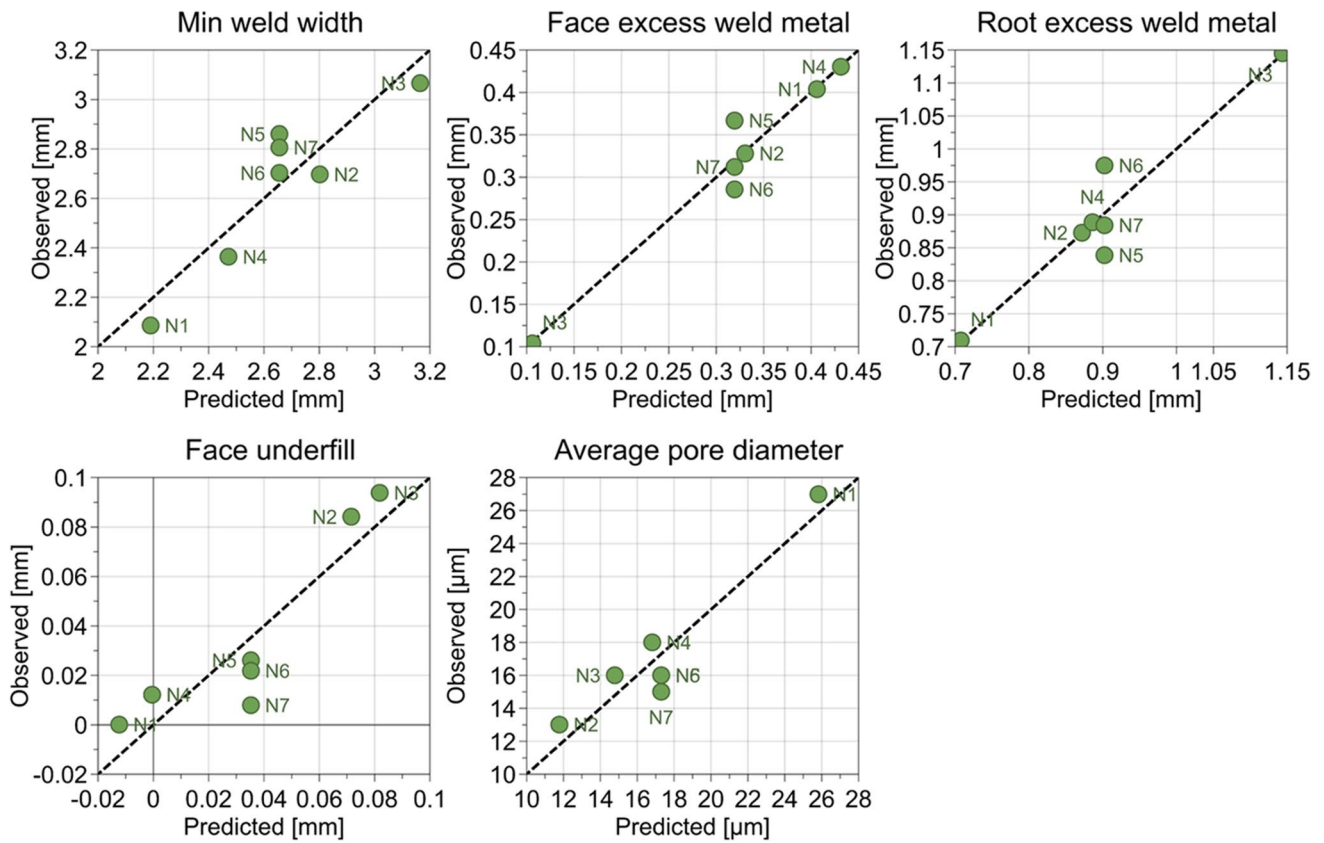
Fig. 5 Comparison of all experimentally measured weld geometry and weld defects with the predicted weld geometry and defects from the regression model

Table 6 R^2 and p-values of regression models calculated using Modde software for the responses (Wm, face and root excess weld metal, face underfill, and average pore diameter)

Response	R^2	p-value of the regression model (from ANOVA table)
Wm	0.829	0.114
Face excess weld metal	0.951	0.018
Root excess weld metal	0.910	0.045
Face underfill	0.814	0.332
Average pore diameter	0.883	0.065

size of the as-received base material is around 55–60 µm or ASTM 5–5.5. Bright and dark particles, identified as Nb-rich carbide containing Ti and C, i.e., (Nb,Ti)C and Ti–rich nitride containing Nb and N, i.e., (Ti,Nb)N by SEM–EDS analysis, respectively, are observed in the base metal microstructure. One example of the typical EDS profiles and corresponding chemical compositions of (Nb,Ti)C and (Ti,Nb)N found in the base material microstructure is displayed in Fig. 7 and Table 7, respectively. The presence of Nb-rich carbide and Ti–rich nitride in VDM Alloy 780 is also reported by Sharma et al. [16]. Note that it is not possible to measure the concentrations of C and N by SEM–EDS analysis quantitatively; therefore, both elements are excluded from the analysis. It is revealed in the higher magnification BSE image (Fig. 6b) that (Ti,Nb)N particles are associated with (Nb,Ti)C in a single body. In addition, fine γ′ with the size of ~ 10 nm or less are present uniformly throughout the microstructure (Fig. 8).

3.2.2 FZ microstructure

Figure 9a shows the low magnification SEM-BSE image of the as-polished FZ microstructure consisting of a cellular-dendritic structure. A higher magnification image (Fig. 9b) displays a high number density of microconstituents present in the interdendritic region imaged in bright contrast. SEM–EDS analysis in higher magnification (Fig. 9c) reveals two types of microconstituents, i.e., particle A, which exhibits blocky and rod-like morphologies, and particle B, which has an irregular shape distributed semi-continuously in the interdendritic region. Examples of particles A and B's chemical compositions are depicted in Table 8 based on SEM–EDS analysis. The SEM–EDS

Fig. 6 SEM images of base material microstructure of as-received VDM Alloy 780 observed on the etched surfaces showing the presence of (Nb,Ti)C and (Ti,Nb)N in (**a**) low magnification and (**b**) higher magnification (BSE images)
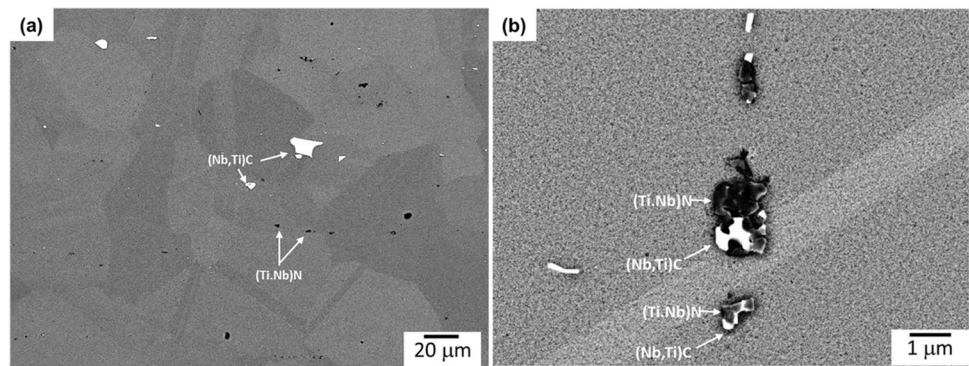

Fig. 7 Typical EDS profile of (**a**) (Nb,Ti)C, (**b**) (Ti,Nb)N, and (**c**) matrix in the base metal microstructure of VDM Alloy 780
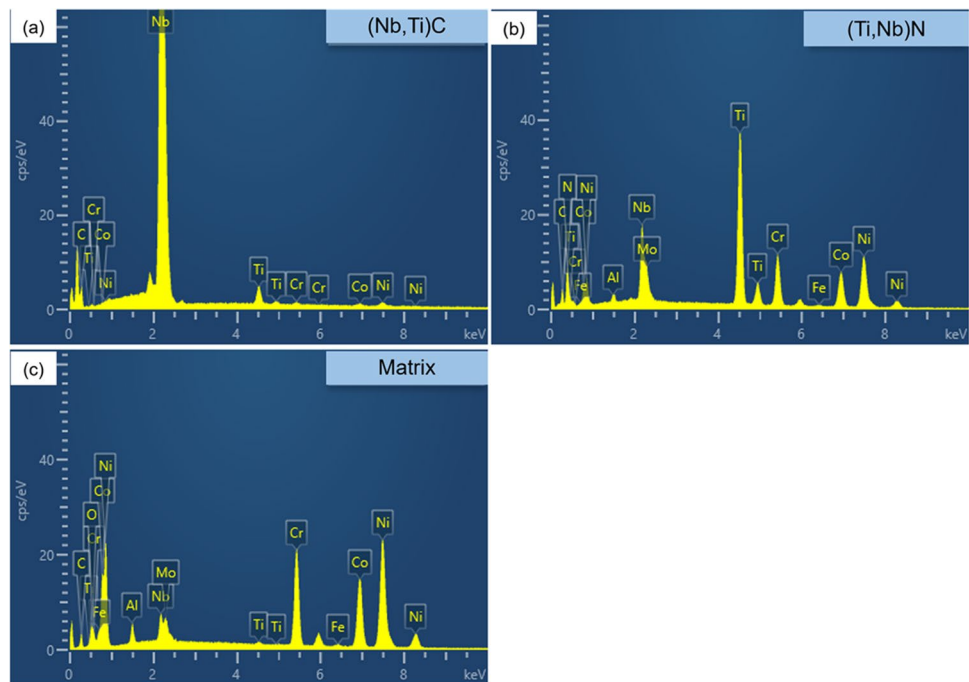

Table 7 Chemical composition of (Nb,Ti)C, (Ti,Nb)N, and matrix obtained from semi-quantitative SEM–EDS point analysis

Element (wt%)	Al	Ti	Cr	Fe	Co	Ni	Nb	Mo
(Nb,Ti)C	0.05	4.86	0.34	0.00	0.00	1.83	92.93	0.00
(Ti,Nb)N	0.13	56.19	1.75	0.00	2.94	5.32	33.67	0.00
Matrix	1.96	0.23	16.35	0.66	24.17	49.25	4.82	2.55

analysis suggests that particle A appears to be (Nb,Ti) C-type carbide. The blocky and rod-like morphologies are also typical for MC carbide in precipitation-hardening superalloys [17–20]. Meanwhile, irregular-shaped particle B exhibits eutectic-type morphology, which is the typical morphology of γ/Laves eutectics constituent found in other Nb-carrying superalloys such as alloy 718 and ATI 718Plus [21–23]. Note that VDM Alloy 780 is also an Nb-carrying superalloy with the Nb content almost identical to alloy 718 and ATI 718Plus. It is observed that the chemical composition of particle B has a substantial similarity

with γ/Laves eutectics in alloy 718 and ATI 718Plus, in terms of Nb, Mo, Cr, and Ni enrichments. Particle B also seems to contain Fe and Ti to a much lower extent than alloy 718 and ATI 718Plus. This is likely due to lower Fe and Ti concentration in VDM Alloy 780 compared to alloy 718 and ATI 718Plus. Therefore, particle B appears to be γ/Laves eutectics type constituent based on the morphology and the SEM–EDS analysis. Table 8 also shows that γ/Laves eutectics constituent in the FZ of VDM Alloy 780 exhibits a high Co concentration of about 23 wt%, which is close to the nominal Co content in the alloy (24.17% wt%).
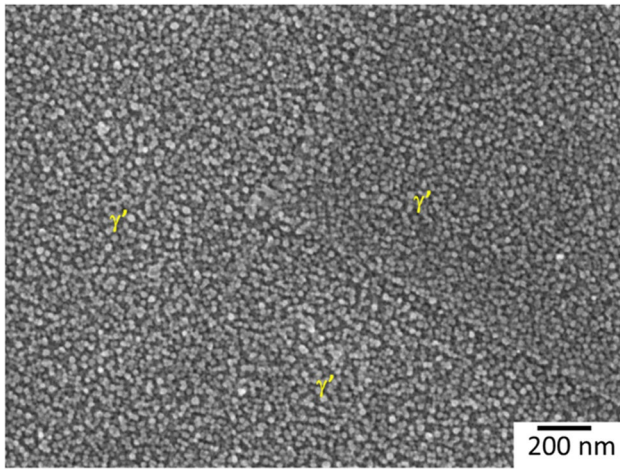
Fig. 8 High-magnification SEM image showing high number density of fine γ′ in the base material microstructure of as-received VDM Alloy 780 (SE in-lens image)

This behavior resembles the Co concentration of γ/Laves eutectics in ATI 718Plus (7.59 wt%), which is close to the nominal Co content in the alloy (8.9 wt%) as reported by Andersson et al. [24].

Figure 10a shows a high-resolution SEM in-lens image of γ/Laves eutectic in the interdendritic region of the electrolytically etched sample. Interestingly, a high number density of plate-like phase was revealed surrounding the γ/Laves eutectics after etching. Because of the extremely fine size of

the plate-like phase, it is impossible to analyze the phase's chemical composition using SEM–EDS. The presence of plate-like precipitates surrounding the interdendritic Laves eutectic constituents is reported in the FZ of TIG-welded [25], and the deposit of WAAM-built [26] ATI 718Plus by Asala et al. The plate-like phase is identified as η-phase using TEM selected area diffraction pattern by the same authors and found to be enriched in Ni, Nb, Al, and Ti from the TEM-EDS analysis. In VDM Alloy 780 itself, plate-like precipitates are reported in the fully heat-treated condition by Ghica et al. [2] using HRTEM characterization, and they exhibit a layered structure composed of alternating η and δ thin stripes. Interestingly, Ghica et al. also found that the plate-like phase in fully heat-treated VDM Alloy 780 is enriched in Ni, Nb, Al, and Ti, similar to those reported by Asala et al. [25, 26] in as-welded and as-built ATI 718Plus. Therefore, there is a possibility that the plate-like precipitates present in the surrounding of γ/Laves eutectics in the FZ of VDM Alloy 780 are η/δ phase, further TEM investigation would however be necessary to confirm this.

A high magnification image (Fig. 10b) of the region marked in Fig. 10a reveals the existence of fine γ′ precipitates in the γ phase within and immediately adjacent to the Laves particle. The spherical morphology of γ′ particles suggests that γ′ precipitates are likely formed through solid-state precipitation during cooling and not by solidification reaction. The γ′ phase that forms as solidification product, i.e., γ-γ′ eutectics, typically has an irregular shape as reported in other superalloys [17, 27, 28]. The presence of γ′ particles is

Fig. 9 SEM-BSE images of fusion zone; (**a**) low-magnification image showing cellular-dendritic microstructure; (**b**) higher magnification image from a region marked in (**a**) showing the presence of microconstituents in the interdendritic regions; (**c**) higher magnification image marked in (**b**) showing the morphology of different types of interdendritic microconstituents, i.e., particle A is (Nb,Ti)C, while particle B is γ/Laves eutectics
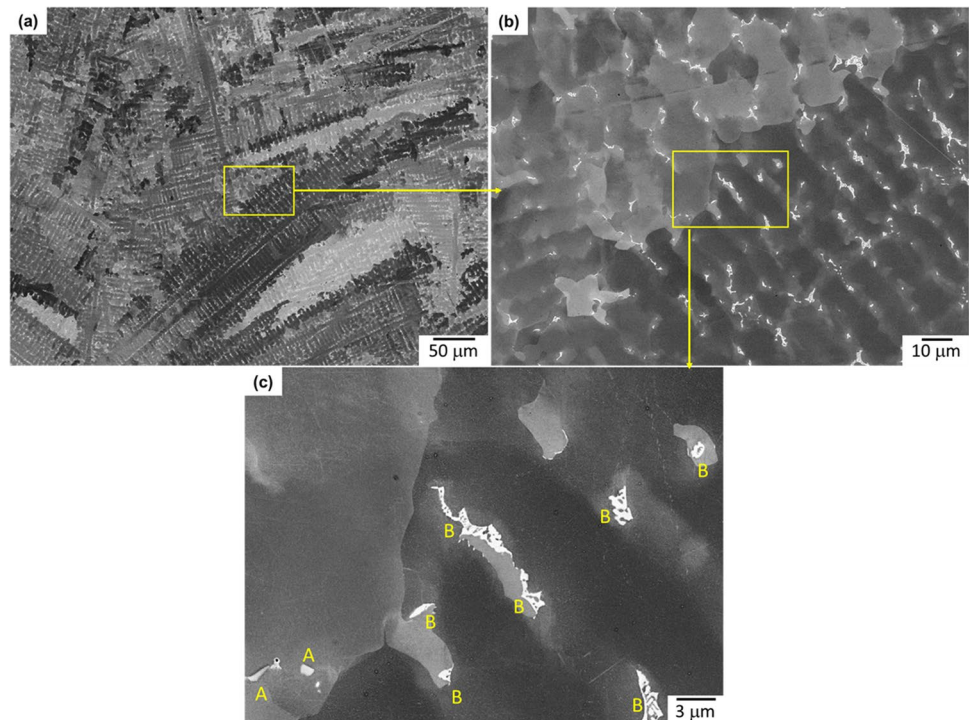
Table 8 Chemical composition of interdendritic microconstituents (particles A and B) in the FZ obtained from semi-quantitative SEM–EDS point analysis

Element (wt%)	Al	Ti	Cr	Fe	Co	Ni	Nb	Mo
Particle A	0.41	6.12	3.88	0.24	1.87	4.96	82.09	0.44
Particle B	0.98	0.40	12.01	0.50	22.93	38.40	21.60	3.20
Interdendritic γ	2.09	0.32	18.18	0.23	23.71	46.68	5.99	2.80
γ/Laves eutectic in FZ of alloy 718 [21]	-	2.0	13.2	11.4	-	48.6	19.1	4.4
γ/Laves eutectic in FZ of ATI 718Plus [24]	1.02	1.35	13.2	6.03	7.59	42.07	20.04	3.65

Fig. 10 (**a**) SEM in-lens image showing γ/Laves eutectic in the interdendritic region of the etched sample; (**b**) higher magnification image of a region marked in (**a**); (**c**) high-magnification image of primary dendrite core.
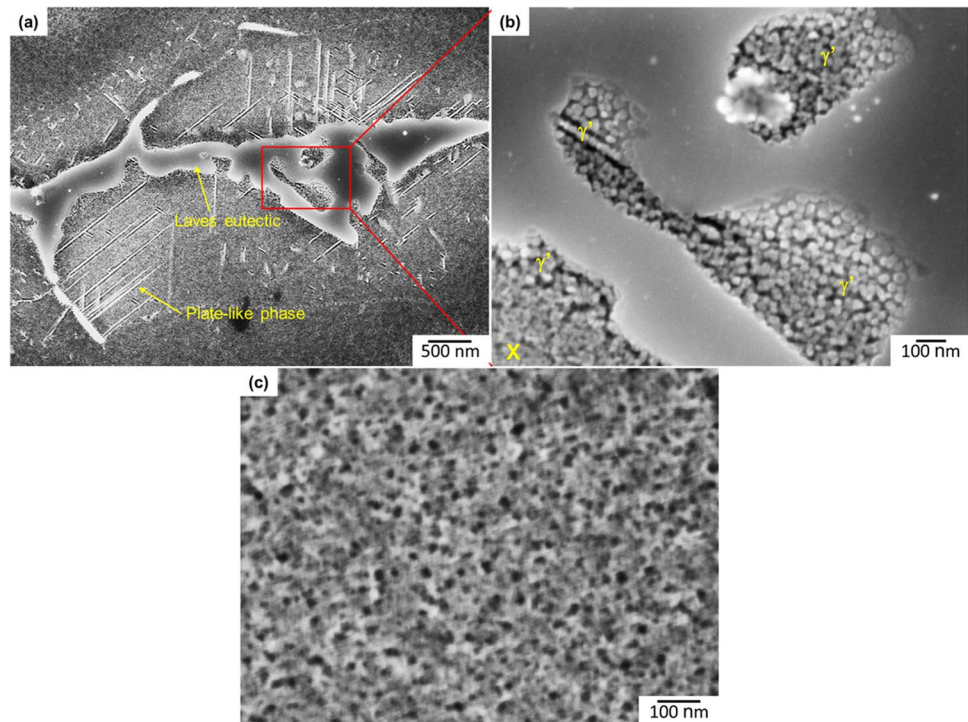
not clearly resolvable from the SEM micrograph in the interdendritic region away from γ/Laves eutectics, as shown in a region marked X in Fig. 10b and the dendrite core (Fig. 10c). This suggests that γ′ precipitates do not form uniformly in the FZ.

In other Nb-bearing superalloys such as alloy 718 and ATI 718Plus, Nb-rich phases such as MC carbide and Laves eutectics in the interdendritic region are generally well-known to form through eutectic reactions during the solidification process due to elemental microsegregation [21, 22, 25, 29, 30]. The formation of both constituents in VDM Alloy 780 may follow a similar solidification reaction sequence as those reported in alloy 718 and ATI 718Plus due to similar Nb and C content in those three alloys. DuPont et al. [30] reported that the general solidification reaction sequence of Nb-bearing Ni-based alloys with a high Nb concentration (> 2 wt%) and low C concentration (< 0.075 wt%)

could be described by a three-step process as follows. Firstly, the solidification is initiated by forming primary γ dendrites via a reaction of L→γ+L, and during the growth of the dendrite, it rejects the solute elements with partition coefficients less than unity to the interdendritic liquid. Once the solubility limit of the solute elements in the interdendritic liquid is surpassed, the formation of secondary solidification microconstituents starts to occur. During the growth of primary dendrite, strong MC carbide forming elements, i.e., Nb and Ti, continuously enrich the interdendritic liquid that may ultimately lead to the formation of MC-type carbides. This is most likely to take place via a univariant eutectic-type reaction of L→γ+MC over a range of temperatures [31]. On further cooling, the residual liquid would continue to get enriched by Nb, which may eventually lead to the formation of Laves eutectics via a reaction of L→γ+Laves over a range of temperatures due to the supersaturation of Nb.

Thermodynamics simulation by Thermo-Calc (Thermo-Calc 2020a version) using the TTNI8 (ThermoTech Ltd.) database for commercial Ni-based superalloys based on the classic Scheil solidification module assuming no back diffusion in the solid (Fig. 11) shows that the liquid is enriched with Nb and Ti atoms as the solidification progressed in VDM Alloy 780, suggesting Nb and Ti segregate into the liquid during the weld solidification that ultimately may result in the formation of Nb-rich MC carbide and Laves phase through eutectic reactions as previously described. Meanwhile, it is still unclear whether the plate-like phase surrounding the Laves phase particles in the FZ of VDM Alloy 780 was formed through solidification or precipitation.

The existence of intermetallic constituents, i.e., Laves phase and plate-like precipitates, in the FZ of VDM Alloy 780 needs careful consideration. Schirra et al. [32] reported in their study on alloy 718 that Laves phase has a weak interface with the γ matrix, and it acts as a preferential site for easy crack initiation and propagation owing to its inherent brittle nature. Furthermore, the formation of Laves eutectic constituents would also cause the matrix a depletion of main alloying elements needed for its strengthening. It is reported by Vishwakarma et al. [29] in their study of as-welded ATI 718Plus that precipitation of the primary strengthening phase γ′, which contains a notable amount of Nb (approximately 14 wt.%), in FZ was restricted owing to the Laves phase formation. Regarding the plate-like precipitates, their presence in the interdendritic region may also significantly deteriorate the mechanical properties of the weldment, especially on the notch sensitivity and intergranular fatigue crack resistance [26]. Recall that γ′ precipitates do not form homogeneously in the FZ of VDM Alloy 780. Inhomogeneous distribution of γ′ may negatively influence the mechanical

properties at high temperatures [33]. Therefore, a suitable PWHT is needed to eliminate Laves and plate-like phases and produce uniform precipitation of γ′ particles.

In general, the FZ microstructure of welded Nb-bearing superalloys may also be influenced by the welding parameters, which are connected with the heat input, and, ultimately, the weld cooling rate. Manikandan et al. [34] reported that a reduction in weld cooling rate weakens the Nb segregation, decreases the formation of Laves phase, and refines the dendrite arm spacings in Alloy 718. In ATI 718Plus, it is reported by Asala et al. [25] that γ′/γ″ and δ/ηphases are found apart from Laves phase and NbC in the TIG welded FZ microstructure. However, Vishwakarma et al. [29] reported that only Laves phase and NbC are present in the FZ of the electron beam (EB)–welded ATI 718Plus. Note that the heat input of EBW is much lower than TIG welding, resulting in a much faster cooling rate in EBW. EBW is also reported to form Laves phase with a lower Nb content than TIG welding in the FZ of Alloy 718 [35]. However, in this work, as mentioned in Sect. 2.4, there are no notable microstructural differences in terms of the type, size, morphology, and number density of constituents, dendrite arm spacings, and Nb-content in Laves phase in the samples welded using the highest and lowest heat input covered in the DOE. This suggests that the samples produced in all the DOE runs exhibit similar as-welded FZ microstructure. The similarity in the FZ microstructure in all samples is plausible due to reasonably narrow welding parameter windows used in the DOE, i.e., welding current of 480–490 A and travel speed of 8–9 mm/s. The fairly narrow parameter windows produced heat inputs that arguably led to a comparable cooling rate in all samples during the weld solidification, resulting in no distinct microstructural difference in the FZ of all samples.
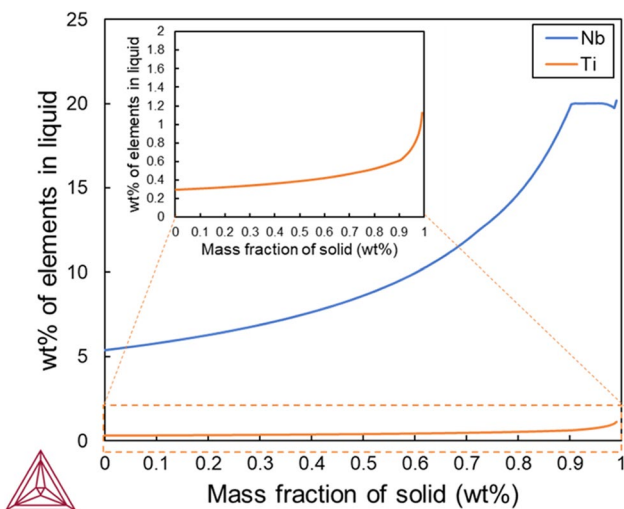
3.2.3 HAZ microstructure

The HAZ microstructure of welded VDM Alloy 780 directly adjacent to the fusion boundary consists of a partially melted zone, i.e., PMZ (Fig. 12a), with numerous liquated and resolidified regions in the grain interior and grain boundary. PMZ has been described as the area outside the FZ where liquation happens during welding because heating exceeds the equilibrium solidus temperature of the alloy [22].

Most of the liquated and resolidified matrix and grain boundaries in the PMZ show different compositional contrast with respect to the unmelted matrix in the SEM-BSE image. Microconstituents imaged in bright contrast are also present in the liquated and resolidified regions. Based on the SEM–EDS analysis, the first microconstituent is found to be rich in Nb and contains a small amount of Ti, while the other one is found to be enriched in Nb, Mo, Ti, Ni, Co, and Cr, suggesting that they are likely

Fig. 11 Thermo-Calc simulation showing the enrichment of Nb and Ti in the liquid during solidification of VDM Alloy 780

Fig. 12 (**a**) SEM-BSE image showing (Nb,Ti)C particles and γ/Laves eutectic in the resolidified regions in PMZ; (**b**) higher magnification image of a region marked in (**a**) depicting Laves phase particle and plate-like precipitates surrounding it.
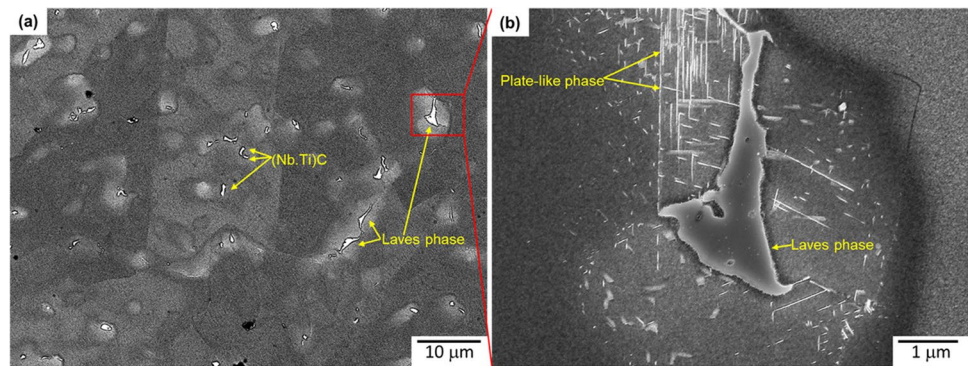
to be (Nb,Ti)C and Laves phase particles, respectively, that are formed as resolidified eutectics from the former PMZ liquid. Furthermore, a high magnification image of a region marked in Fig. 12a as shown in Fig. 12b reveals that plate-like precipitates are present surrounding the Laves phase particle, which is similar to the observation made in FZ. Thus, it is probable that the solidification behavior of liquid in PMZ, to some extent, is likely to follow a similar pattern to the one observed in FZ. The initial solid to form from the PMZ liquid would be γ solid solution followed by γ/(Nb,Ti)C eutectic and γ/Laves eutectic reactions, as observed in the HAZ microstructure. As in FZ, the formation of plate-like precipitates surrounding the Laves particle in HAZ is still unclear, whether through solidification or precipitation reaction.

In addition, constitutional liquation of (Nb,Ti)C particles on grain boundary is observed in HAZ. Constitutional liquation happens because of incomplete solid-state dissolution of secondary phase particles under nonequilibrium rapid heating conditions during welding. This situation leads to a compositional gradient on the matrix interface in equilibrium with the particle. The interface starts to melt and forms a liquid when the temperature during the welding heating cycle reaches the eutectic temperature of the system. Therefore, liquid exists due to constitutional liquation of secondary phase particles below the equilibrium solidus temperature of the alloy. Figure 13 shows an SEM-BSE image of liquated (Nb,Ti)C in HAZ further away from the fusion boundary with a resolidified eutectic-like product at the (Nb,Ti)C-matrix interface. SEM–EDS point analysis (Table 9) shows that the resolidified product appeared to be γ/Laves eutectic-type constituent. Constitutional liquation of Nb-rich MC carbide with γ/Laves eutectic as the resolidified product has been reported in numerous studies in welding similar Nb-bearing superalloys, i.e., alloy 718 [36–39] and ATI 718Plus [18, 30, 40], and may lead to HAZ cracking. However, in this study, no cracking occurred in the K-TIG bead-on-plate weld of VDM Alloy 780.
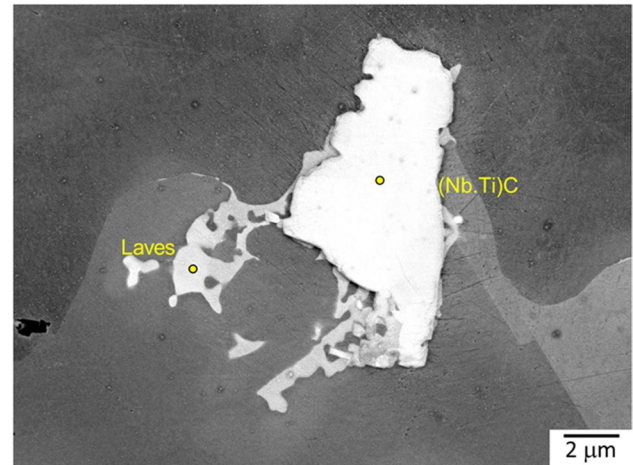

Fig. 13 SEM-BSE image showing constitutional liquation of (Nb,Ti)C particle in HAZ further away from the fusion boundary and its association with γ/Laves eutectic constituent (as-polished sample)

4 Conclusions

1. All K-TIG welding DOE runs of VDM Alloy 780 produced welds with Wm larger than 1.5 mm, face underfill, face and root excess weld metal, and average pore diameter below the maximum acceptable limit stipulated in AWS D17.1 M:2010 for aerospace applications.
2. No cracks are found in the FZ and HAZ.
3. Travel speed significantly influences the Wm, face and root excess weld metal, face underfill, and average pore diameter. Welding current and the interaction current*travel speed significantly influence the face and root excess weld metal, respectively.
4. Microconstituents in the interdendritic regions of FZ are identified as (Nb,Ti)C particles and γ/Laves eutectic constituents based on SEM–EDS analysis, suggesting elemental microsegregation during the weld solidification. In addition, plate-like precipitates likely to be η/δ phase are also observed surrounding the interdendritic Laves eutectic constituents. γ′ particles are found to be inhomogeneously precipitated in the FZ.

Table 9 Chemical composition of liquated Nb-rich carbide and the associated Laves phase as the resolidified product in the HAZ obtained from semi-quantitative SEM–EDS point analysis

Element (wt%)	Al	Ti	Cr	Fe	Co	Ni	Nb	Mo
(Nb,Ti)C	0.06	2.54	0.47	0.00	1.07	1.31	94.55	0.00
Laves phase	0.43	0.34	10.33	0.15	23.86	30.46	29.49	4.94

5. Suitable PWHT is needed to eliminate Laves and plate-like phases and produce uniform precipitation of γ′ particles in the FZ.

6. In HAZ directly adjacent to the fusion boundary where equilibrium supersolidus melting occurs, i.e., PMZ, (Nb,Ti)C, Laves phase, and plate-like particles are found in the liquated and resolidified regions, suggesting the solidification behavior in HAZ to some extent is likely to follow a similar pattern to the one observed in FZ.

7. Constitutional liquation of (Nb,Ti)C particle in HAZ further away from the fusion boundary is observed. The liquated (Nb,Ti)C appears to be associated with the γ/ Laves eutectic as the resolidified product.

Declarations

Conflict of interest The authors declare no competing interests.

References

1. Bergner M, Rösler J, Gehrmann B, Klöwer J (2018) Effect of heat treatment on microstructure and mechanical properties of VDM Alloy 780 Premium. Proceedings of the 9th International Symposium on Superalloy 718 & Derivatives: Energy, Aerospace, and Industrial Applications, Springer 489–499. https://doi.org/10.1007/978-3-319-89480-5_31.

2. Ghica C, Solis C, Munke J, Stark A, Gehrmann B, Bergner M, Rösler J, Gilles R (2020) HRTEM analysis of the high-temperature phases of the newly developed high-temperature Ni-base superalloy VDM 780 Premium. J Alloy Compd 814:152157. https://doi.org/10.1016/j.jallcom.2019.152157

3. Solís C, Munke J, Bergner M, Kriele A, Mühlbauer M, Cheptiakov D, Gehrmann B, Rösler J, Gilles R (2018) In situ characterization at elevated temperatures of a new Ni-based superalloy VDM-780 Premium. Metall and Mater Trans A 49(9):4373–4381. https://doi.org/10.1007/s11661-018-4761-6

4. Rösler J, Hentrich T, Gehrmann B (2019) On the development concept for a new 718-type superalloy with improved temperature capability. Metals 9(10):1130. https://doi.org/10.3390/met9101130

5. Fedorova T, Rösler J, Klöwer J, Gehrmann B (2014) Development of a new 718-type Ni-Co superalloy family for high temperature applications at 750◦ C. MATEC web of conferences, EDP Sciences, 01003. https://doi.org/10.1051/matecconf/20141401003.

6. Andersson J (2011) Weldability of precipitation hardening superalloys–influence of microstructure. Dissertation, Chalmers University of Technology

7. Andersson J (2018) Review of weldability of precipitation hardening Ni-and Fe-Ni-based superalloys. Proceedings of the 9th International Symposium on Superalloy 718 & Derivatives: Energy, Aerospace, and Industrial Applications, 899–916. https://doi.org/10.1007/978-3-319-89480-5_60.

8. Liu Z, Fang Y, Cui S, Luo Z, Liu W, Liu Z, Jiang Q, Yi S (2016) Stable keyhole welding process with K-TIG. J Mater Process Technol 238:65–72. https://doi.org/10.1016/j.jmatprotec.2016.07.005

9. Fei Z, Pan Z, Cuiuri D, Li H, Wu B, Ding D, Su L, Gazder AA (2018) Investigation into the viability of K-TIG for joining armour grade quenched and tempered steel. J Manuf Process 32:482–493. https://doi.org/10.1016/j.jmapro.2018.03.014

10. Kuzmikova L, Larkin N, Pan Z, Callaghan M, Li H, Norrish J (2012). Investigation into feasibility of hybrid laser-GMAW process for welding high strength quenched and tempered steel

11. Fei Z, Pan Z, Cuiuri D, Li H, Van Duin S, Yu Z (2019) Microstructural characterization and mechanical properties of K-TIG welded SAF2205/AISI316L dissimilar joint. J Manuf Process 45:340–355. https://doi.org/10.1016/j.jmapro.2019.07.017

12. Khan A., Hilton P., Blackburn J., Allen C (2012) Meeting weld quality criteria when laser welding Ni-based alloy 718. International Congress on Applications of Lasers & Electro-Optics, Laser Institute of America, 549–557. https://doi.org/10.2351/1.5062506.

13. Eriksson L, Johansson E, Kettaneh-Wold N, Wikström C (2000) Wold S, Design of experiments, principles and applications. Learn ways AB, Stockholm.

14. Alvarez P, Vázquez L, Ruiz N, Rodríguez P, Magaña A, Niklas A, Santos F (2019) Comparison of hot cracking susceptibility of TIG and laser beam welded alloy 718 by varestraint testing. Metals 9(9):985. https://doi.org/10.3390/met9090985

15. Sharma J, Haghighat MH, Gehrmann B, Moussa C, Bozzolo N (2020) Dynamic and post-dynamic recrystallization during

supersolvus forging of the new nickel-based superalloy—VDM Alloy 780. Superalloys 2020:450–460. https://doi.org/10.1007/978-3-030-51834-9_44

16. Abedi H, Ojo O (2022) Microstructural analysis of fusion zone in gas tungsten arc-welded newly developed Co-based superalloy. Metall and Mater Trans A 53(2):377–381. https://doi.org/10.1007/s11661-021-06541-w

17. Hanning F, Khan AK, Andersson J, Ojo O (2020) Advanced microstructural characterization of cast ATI 718Plus®—effect of homogenization heat treatments on secondary phases and repair welding behaviour. Welding in the World 64(3):523–533. https://doi.org/10.1007/s40194-020-00851-0

18. Ariaseta A, Kobayashi S, Takeyama M, Wang Y, Imano S (2020) Characterization of recrystallization and second-phase particles in solution-treated additively manufactured alloy 718. Metall and Mater Trans A 51(2):973–981. https://doi.org/10.1007/s11661-019-05560-y

19. Otsuka T, Wakabayashi D, Igarashi D, Ariaseta A, Imano S, Wang Y, Kobayashi S, Takeyama M (2018) Effect of homogenization on creep of additive manufactured alloy 718, Proceedings of the 9th International Symposium on Superalloy 718 & Derivatives: Energy, Aerospace, and Industrial Applications, Springer, 501–513. https://doi.org/10.1007/978-3-319-89480-5_32.

20. Cieslak M, Knorovsky G, Headley T, Romig Jr A (1989) The solidification metallurgy of alloy 718 and other Nb-containing superalloys, Sandia National Lab.(SNL-NM), Albuquerque, NM (United States).

21. Knorovsky G, Cieslak M, Headley T, Romig A, Hammetter W (1989) Inconel 718: a solidification diagram. Metall Trans A 20(10):2149–2158. https://doi.org/10.1007/BF02650300

22. Singh S, Andersson J (2019) Varestraint weldability testing of cast ATI® 718Plus™—a comparison to cast Alloy 718. Welding in the World 63(2):389–399. https://doi.org/10.1007/s40194-018-0626-2

23. Andersson J, Sjöberg G, Viskari L, Brederholm A, Hänninen H, Knee C (2008) Hot cracking of Allvac 718Plus, alloy 718 and Waspaloy at varestraint testing. 47th Conference of Metallurgists (COM) 2008 in Honour of Dr. Mahesh Chaturvedi, Winnipeg, Manitoba, Canada, 24–27 August, 2008, Canadian Institute of Mining, Metallurgy and Petroleum, pp. 401–413.

24. Asala G, Andersson J, Ojo OA (2016) Precipitation behavior of γ′ precipitates in the fusion zone of TIG welded ATI 718Plus®. Int J Advd Manufact Technol 87(9):2721–2729. https://doi.org/10.1007/s00170-016-8642-0

25. Asala G, Khan A, Andersson J, Ojo O (2017) Microstructural analyses of ATI 718Plus® produced by wire-ARC additive manufacturing process. Metall and Mater Trans A 48(9):4211–4228. https://doi.org/10.1007/s11661-017-4162-2

26. Ojo O, Richards N, Chaturvedi M (2006) Study of the fusion zone and heat-affected zone microstructures in tungsten inert gas-welded INCONEL 738LC superalloy. Metall and Mater Trans A 37(2):421–433. https://doi.org/10.1007/s11661-006-0013-2

27. Ojo O, Richards N, Chaturvedi, (2004) Microstructural study of weld fusion zone of TIG welded IN 738LC nickel-based superalloy. Scripta Mater 51(7):683–688. https://doi.org/10.1016/j.scriptamat.2004.06.013

28. Manikandan SGK, Sivakumar D, Rao KP, Kamaraj M (2014) Effect of weld cooling rate on Laves phase formation in Inconel 718 fusion zone. J Mater Process Technol 214(2):358–364. https://doi.org/10.1016/j.jmatprotec.2013.09.006

29. Radhakrishna CH, Prasad Rao K (1997) The formation and control of Laves phase in superalloy 718 welds. J Mater Sci 32(8):1977–1984. https://doi.org/10.1023/A:1018541915113

30. Radhakrishnan B, Thompson R (1989) Solidification of the nickel-base superalloy 718: a phase diagram approach. Metall Trans A 20(12):2866–2868. https://doi.org/10.1007/BF02670181

31. Schirra JJ, Caless RH, Hatala RW (1991) The effect of Laves phase on the mechanical properties of wrought and cast+ HIP Inconel 718. Superalloys 718(625):375–388

32. Strum M, Summers L, Morris J Jr (1983) The aging response of a welded iron-based superalloy. Weld J 62:235–242

33. Chaturvedi MC (2007) Liquation cracking in heat affected zone in Ni superalloy welds. Materials Science Forum, Trans Tech Publ 1163–1170. https://doi.org/10.4028/www.scientific.net/MSF.546-549.1163

34. Vishwakarma K, Richards N, Chaturvedi M (2008) Microstructural analysis of fusion and heat affected zones in electron beam welded ALLVAC® 718PLUS™ superalloy. Mater Sci Eng, A 480(1–2):517–528. https://doi.org/10.1016/j.msea.2007.08.002

35. DuPont JN, Notis M, Marder A, Robino C, Michael J (1998) Solidification of Nb-bearing superalloys Part I Reaction sequences. Metal Mater Trans A 29(11):2785–2796. https://doi.org/10.1007/s11661-998-0319-3

36. Radhakrishnan B, Thompson R (1991) A phase diagram approach to study liquation cracking in alloy 718. Metall Trans A 22(4):887–902. https://doi.org/10.1007/BF02658999

37. Thompson R, Radhakrishnan B, and Mayo D (1989) Intergranular liquid formation, distribution, and cracking. Superalloy 718-Metallurgy and Applications 437–455.

38. Thompson E (1969) Hot cracking studies of alloy 718 weld HAZ. Weld J 48(2):70–79

39. Vishwakarma K (2008) Microstructural analysis of weld cracking in 718 Plus superalloy. Dissertation, University of Manitoba